

RDDM: PRACTICING RAW DOMAIN DIFFUSION MODEL FOR REAL-WORLD IMAGE RESTORATION

Yan Chen^{1*}, Yi Wen^{1*}, Wei Li^{1†}, Junchao Liu¹, Yong Guo², Jie Hu¹, Xinghao Chen¹

¹ Huawei Noah's Ark Lab

² Max Planck Institute for Informatics

{chenyan176, wenyi14, wei.lee}@huawei.com

(a) Real-World Image Restoration Results Starting from Sensor RAW



(b) Comparison with Two-Stage ISP+IR Models

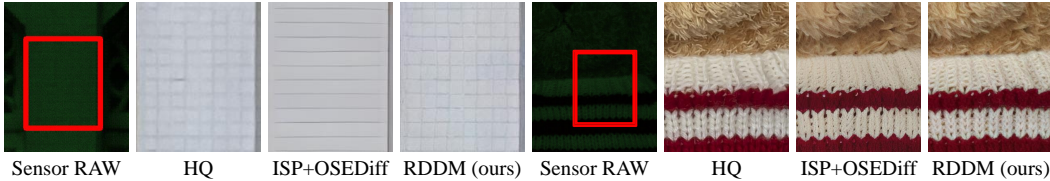


Figure 1: RDDM, restoring directly from the sensor RAW data, demonstrates remarkable results shown in (a), capitalizing on the unprocessed and detail-rich signal. Compared with the two-stage baseline in (b), RDDM delivers markedly higher fidelity and perceptual quality.

ABSTRACT

We present the RAW domain diffusion model (RDDM), an end-to-end diffusion model that restores photo-realistic images directly from the sensor RAW data. While recent sRGB-domain diffusion methods achieve impressive results, they are caught in a dilemma between high fidelity and image generation. As these models process lossy sRGB inputs and neglect the accessibility of the sensor RAW images in many scenarios, e.g., in image and video capturing in edge devices, resulting in sub-optimal performance. RDDM obviates this limitation by directly restoring images in the RAW domain, replacing the conventional two-stage image signal processing (ISP)→Image Restoration (IR) pipeline. However, a simple adaptation of pre-trained diffusion models to the RAW domain confronts many challenges. To this end, we propose: (1) a RAW-domain VAE (RVAE), encoding sensor RAW and decoding it into an enhanced linear domain image, to solve the out-of-distribution (OOD) issues between the different domain distributions; (2) a configurable multi-bayer (CMB) LoRA module, adapting diverse RAW Bayer patterns such as RGGB, BGGR, etc. To compensate for the deficiency in the

*Equal Contribution.

†Project Lead.

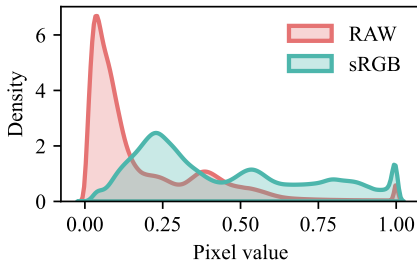


Figure 2: Distribution gap between RAW and sRGB images.

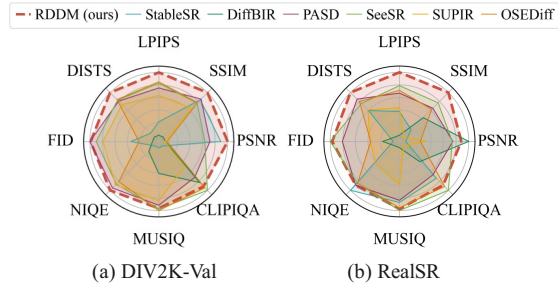


Figure 3: The performance comparison among SD-based methods on test datasets DIV2K-Val, and RealSR, respectively.

dataset, we develop a scalable data synthesis pipeline synthesizing RAW LQ-HQ pairs from existing sRGB datasets for large-scale training. Extensive experiments demonstrate RDDM’s superiority over state-of-the-art sRGB diffusion methods, yielding higher fidelity results with fewer artifacts. Codes will be publicly available at github.com/YanCHEN-fr/RDDM.

1 INTRODUCTION

Real-world Image Restoration (Real-IR) aims to restore high-quality (HQ) images from low-quality (LQ) images containing complex degradations Fan et al. (2020); Zhang et al. (2022); Jinjin et al. (2020); Zhang et al. (2019; 2018b; 2017). Real-IR has transitioned from GAN-based adversarial training Ledig et al. (2017); Wang et al. (2018); Xie et al. (2023) to leveraging the powerful generative priors of text-to-image (T2I) diffusion models Zhang et al. (2023); Lin et al. (2024); Wang et al. (2024); Wu et al. (2024b); Yu et al. (2024). Despite their success in the sRGB domain, these methods encounter a fundamental bottleneck: the Image Signal Processor (ISP) irreversibly discards critical details and compresses the dynamic range from high-bit (12-14 bits) RAW images into 8-bit sRGB images. Restoring HQ images from such degraded sRGB inputs inevitably leads to sub-optimal results Nguyen & Brown (2016); Xing et al. (2021).

To transcend the performance ceiling of Real-IR, shifting restoration to the sensor RAW domain, i.e. the front-end of ISP, holds substantial promises. RAW data preserves the original optical and physical signals, offering higher bit depth and richer information. Nevertheless, integrating T2I models into the RAW domain is confronted with two critical challenges: (1) **Distribution Disparity**: the significant gaps in the luminance and mosaic patterns between the sRGB and RAW images, as shown in Fig.2, make direct application of T2I models in the RAW domain ineffective. (2) **Generalization Constraints**: varying sensor Bayer patterns and noise characteristics hinder the ability of the model to generalize across different devices.

In this paper, we propose the RAW Domain Diffusion Model (RDDM), the first practical diffusion-based paradigm for RAW image restoration. To address the aforementioned challenges, we introduce three core innovations:

- **RVAE**: we design a RAW domain Variational Autoencoder (RVAE) using a divide-and-conquer strategy, mapping noisy mosaicked RAW inputs into a latent space and decoding them into enhanced linear images to bridge the RAW-sRGB distribution gap.
- **CMB-LoRA**: a sensor-aware adaptation module that strategically selects LoRA weights to handle heterogeneous Bayer patterns, significantly enhancing cross-sensor generalization.
- **RAW Image Synthesis Pipeline**: to overcome data scarcity, we propose a synthesis method to generate high-fidelity RAW-linear pairs from large-scale sRGB datasets.

Extensive experiments demonstrate that RDDM achieves state-of-the-art fidelity and generative performance, as illustrated in Fig. 3.

2 RELATED WORK

Real-world Image Restoration. Since the advent of ESRGAN Ledig et al. (2017), Real-IR has evolved from GAN-based approaches Ledig et al. (2017); Wang et al. (2018; 2021); Zhang et al. (2021); Liang et al. (2022); Chen et al. (2022), which often suffer from training instability and unnatural artifacts, to diffusion-based models. By leveraging pre-trained Stable Diffusion (SD) priors, the latter achieve superior visual realism and texture generation through various condition injection strategies Podell et al. (2023); Rombach et al. (2022); Wang et al. (2024); Wu et al. (2024b); Yu et al. (2024). However, existing Real-IR methods perform predominantly in the sRGB domain, where critical sensor-level information is often discarded by the ISP. Furthermore, directly transferring sRGB-trained models to the RAW domain yields poor performance due to severe domain mismatch. This gap necessitates a specialized framework that effectively adapts the generative power of diffusion models to the unique characteristics of RAW data.

Image Processing in RAW Domain. Modern imaging sensors capture RAW data, which is converted to sRGB by a traditional ISP pipeline via sequential modules, including demosaicing (DM), denoising (DN), and tone mapping (TM). Subsequent post-processing (e.g., AWB, clipping) compresses dynamic range, leading to irreversible detail loss in the final sRGB output. One-stage methods Brooks et al. (2019) typically integrate DN and DM but often suffer from over-smoothing due to limited representation capacity. In contrast, integrating diffusion models into the RAW domain harnesses essential sensor signals and enhances generative capacity, providing a superior foundation for high-fidelity image restoration.

3 METHODOLOGY

3.1 PROBLEM MODELING

In the sRGB domain, Real-IR model G_θ^{rgb} , parameterized by θ , aims to estimate HQ sRGB image $\hat{X}_H^{rgb} \in \mathbb{R}^{h \times w \times 3}$ given LQ sRGB image $X_L^{rgb} \in \mathbb{R}^{h \times w \times 3}$. In RAW domain, we train a neural network G_θ^{raw} to transform LQ sensor RAW $X_L^{raw} \in \mathbb{R}^{h \times w \times 1}$ to HQ linear domain image $\hat{X}_H^{lin} \in \mathbb{R}^{h \times w \times 3}$. The training task can be modeled as the following optimization problem:

$$\theta^* = \operatorname{argmin}_\theta \mathbb{E}_{X_L^{raw}, X_H^{lin} \sim S} \left[\mathcal{L}(G_\theta^{raw}(X_L^{raw}, \epsilon), X_H^{lin}) \right] \quad (1)$$

where S is the dataset consisting of (X_L^{raw}, X_H^{lin}) pairs, and \mathcal{L} is the loss function, respectively.

Existing AIGC-based image restoration paradigms typically follow the pipeline illustrated in Fig. 4 (a). The initial sensor RAW is processed through conventional image signal processing, which integrates a denoising, demosaicing module (DDM), and post-tone mapping modules to generate an sRGB image. The AIGC model is subsequently applied to this sRGB output to perform high-quality enhancement. Formally, this paradigm can be expressed as:

$$\hat{X}_H^{rgb} = G_\theta^{rgb}(ISP(X_L^{raw})) \quad (2)$$

In contrast, our proposed RDDM approach, depicted in Fig. 4 (b), bypasses the traditional denoising and demosaicing modules and shifts the AIGC-driven enhancement process into the RAW domain. Following the enhancement, the output of the AIGC model is transformed into the sRGB domain via a post tone mapping (PTP) module. Formally, the RDDM paradigm can be defined as:

$$\hat{X}_H^{rgb} = PTP(G_\theta^{raw}(X_L^{raw})) \quad (3)$$

By operating directly on RAW data, RDDM mitigates the irreversible information loss inherent in standard ISP transformations. Since on-device ISP pipelines are typically proprietary "black boxes," a comprehensive overview of ISP components and their corresponding mathematical derivations is provided in Appendix A.1.

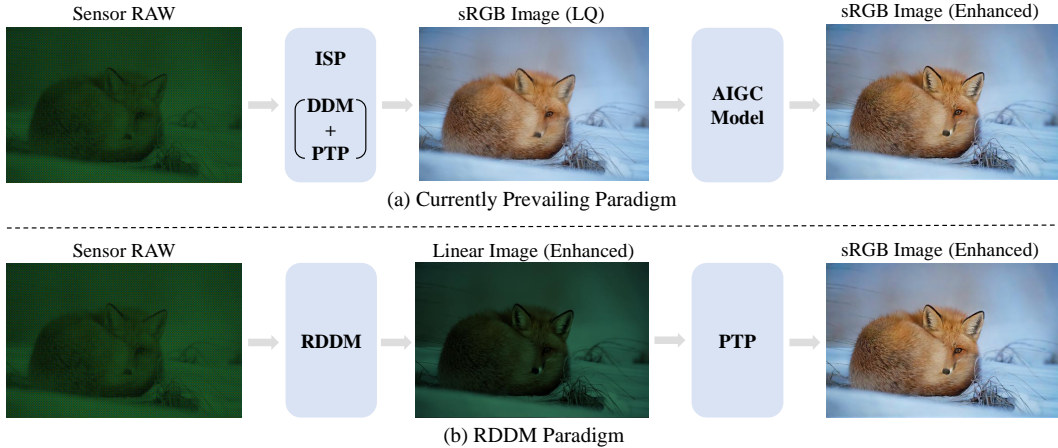


Figure 4: Comparison of Real-IR paradigms. (a) The prevailing paradigm: the restoration process is performed in the sRGB space after the Raw-to-sRGB mapping via an ISP. (b) RDDM paradigm: we perform restoration directly on the RAW data and subsequently map the restored results to the sRGB space using a PTP module.

3.2 RAW DOMAIN DIFFUSION MODEL

Framework Overview. Our framework G_{θ}^{raw} integrates an RVAE and a diffusion network ϵ_{θ} for high-fidelity restoration. Specifically, the encoder E_{θ}^{lin} maps mosaicked RAW inputs into a latent space, where ϵ_{θ} performs iterative refinement to recover fine-grained details. The decoder D_{θ}^{lin} then reconstructs these features into the linear domain, followed by an sRGB transformation via the PTP module. To handle diverse Bayer configurations, we incorporate trainable LoRA layers Hu et al. (2022) into the pre-trained E_{θ}^{lin} and ϵ_{θ} , facilitating adaptive adaptation through our CMB-LoRA strategy. Furthermore, to provide semantic guidance, we employ a DAPE Zheng et al. (2024) to derive textual prompts from sRGB images rendered by the ISP, thereby activating generative priors. An overview of the framework is depicted in Fig. 5.

RAW Domain VAE. Owing to the vast domain shift, existing sRGB domain VAEs fail to reconstruct effectively, resulting in diffusion model-generated images characterized by low visual quality and significant color shifts. Therefore, we devise a RAW domain VAE that encodes RAW images and subsequently decodes the latent representation into a linear domain image. The training of the RVAE is conducted in two distinct stages. To ensure the decoder is capable of reconstructing images in the linear domain, the first stage involves training on a reconstruction task utilizing linear domain images, following the strategy illustrated in Fig. 5 (a). Given a linear domain input X_H^{lin} , the encoder extracts the latent representation z , which is then reconstructed by the decoder as $\hat{X}_H^{lin} = D_{\theta}^{lin}(E_{\theta}^{lin}(X_H^{lin}))$. Furthermore, we devise a differentiable PTP module that simultaneously supervises training in both the sRGB and RAW domains. Similar to LDM Rombach et al. (2022), we use L_1 loss, LPIPS loss, and GAN loss to train the VAE encoder and decoder to generate realistic details of a linear image:

$$\mathcal{L}_{RVAE} = \mathcal{L}_{rec}(\hat{X}_H^{lin}, X_H^{lin}) + \lambda_G \mathcal{L}_{GAN}(\hat{X}_H^{lin}, X_H^{lin}) \quad (4)$$

where $\mathcal{L}_{rec} = \mathcal{L}_1 + \mathcal{L}_{LPIPS}$ and \mathcal{L}_1 is calculated in both the RAW and sRGB domains. $\lambda_G = \frac{\nabla[\mathcal{L}_{rec}]}{\nabla[\mathcal{L}_{GAN}] + 10^{-4}}$ and $\nabla[\cdot]$ represents the gradient of the last layer in the decoder. Following Rombach et al. (2022), to facilitate diffusion model optimization, we normalize the latent distribution to a standard Gaussian. The scaling factor σ is computed over the training samples:

$$\hat{\mu} = \frac{1}{bchw} \sum_{b,c,h,w} z^{b,c,h,w} \quad (5)$$

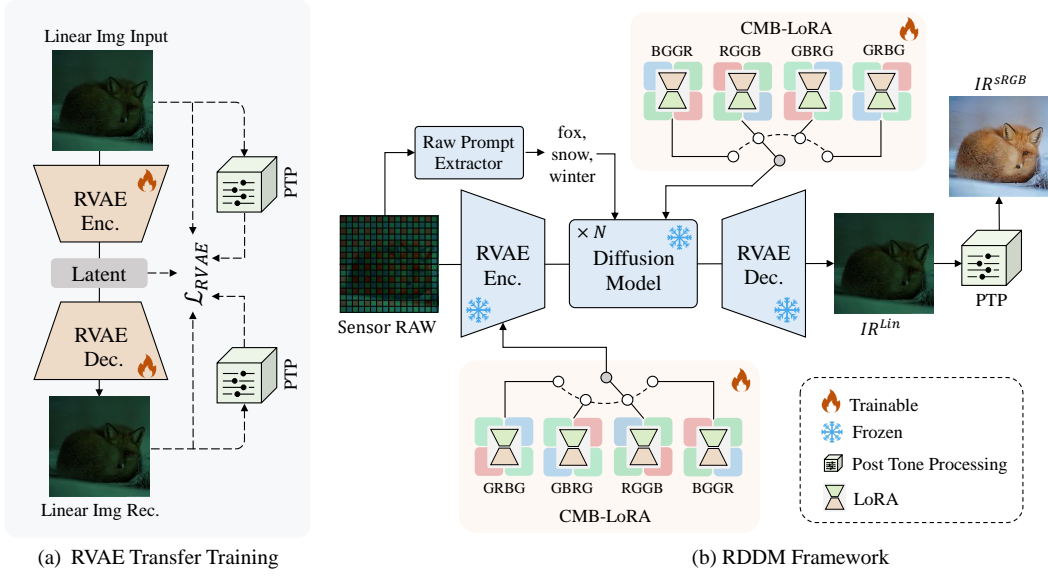


Figure 5: (a) Illustration of RVAE training strategy. (b) RDDM framework. Specifically, it synchronizes the optimization of the CMB-LoRA (within the RVAE encoder) and the pre-trained diffusion network, supervised by RAW-linear image pairs.

$$\sigma^2 = \frac{1}{bchw} \sum_{b,c,h,w} (z^{b,c,h,w} - \hat{\mu})^2 \quad (6)$$

where $z^{b,c,h,w}$ denotes the latent space of the training samples encoded by E_θ^{lin} . $\hat{\mu}$ and σ^2 present the mean and variance of the data distribution. The rescaled latent has unit standard deviation, i.e., $z \leftarrow \frac{z}{\sigma}$. To enable the RVAE to process RAW images, the second training stage involves freezing the encoder and decoder weights optimized in the first stage and incorporating LoRA into the encoder. Concurrently, LoRA modules are integrated into the diffusion model to facilitate the removal of mosaic artifacts and heavy noise while simultaneously enhancing fine-grained image details. The overall training strategy is illustrated in Fig. 5 (b). We use VSD loss, LPIPS loss, and MSE loss to train our model in the RAW domain and the sRGB domain:

$$\begin{aligned} \mathcal{L} = & \mathcal{L}_{VSD}(\hat{X}_H^{lin}, X_H^{lin}) + \lambda_1 \mathcal{L}_{RAW}(\hat{X}_H^{lin}, X_H^{lin}) \\ & + \lambda_2 \mathcal{L}_{RGB}(\mathcal{F}_{PTP}(\hat{X}_H^{lin}), \mathcal{F}_{PTP}(X_H^{lin})) \end{aligned} \quad (7)$$

where λ_1, λ_2 are weighting scalars. $\mathcal{L}_{RAW} = \mathcal{L}_{MSE}$. $\mathcal{L}_{RGB} = \mathcal{L}_{MSE} + \lambda_3 \mathcal{L}_{LPIPS}$. We transform both the model predictions and the ground-truth into the sRGB domain via the proposed PTP module.

CMB-LoRA. To tackle the traditional cross-device generalization challenge posed by diverse Bayer patterns and noise characteristics, we propose Configurable Multi-Bayer (CMB) LoRA. Rather than costly full-parameter retraining, our approach incorporates pattern-specific LoRA branches into the RVAE and diffusion networks. Each branch is independently optimized for a specific Bayer configuration during training and adaptively selected during inference. This parameter-efficient strategy allows our model to handle diverse sensor characteristics without retraining from scratch, as detailed in Fig. 5 (b).

3.3 DATA SYNTHESIS

Despite the prevalence of sRGB datasets for Real-IR (e.g., LSDIR Li et al. (2023), DIV2K Agustsson & Timofte (2017)), a large-scale RAW domain dataset remains absent. To address this deficiency, we construct a large-scale synthetic RAW-domain dataset by applying a degradation pipeline

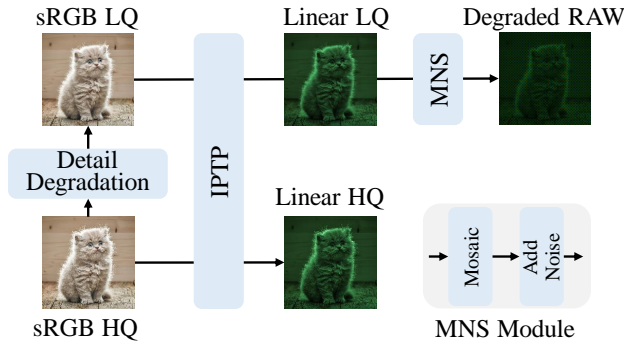


Figure 6: RAW data synthesis pipeline. IPTP transforms an sRGB image into its linear domain counterpart. MNS converts a linear domain image into a sensor RAW image.

to publicly available sRGB resources, thereby facilitating effective training in the RAW domain, as shown in Fig. 6. Following Real-ESRGAN Wang et al. (2021), we first apply detail degradation to obtain X_L^{rgb} from X_H^{rgb} . Crucially, we exclude sRGB-specific JPEG compression and random noise, as these do not align with native sensor characteristics. For stage one training, an inverse post tone processing (IPTP) module projects X_H^{rgb} into the linear domain to obtain the RVAE target X_H^{lin} . In stage two, we synthesize RAW domain LQ inputs X_L^{raw} by passing X_L^{rgb} through the IPTP module and a mosaic noise synthesizer (MNS). Throughout training, X_H^{lin} serves as the ground truth. The process is formulated as:

$$X_H^{lin} = IPTP(X_H^{rgb}), X_L^{raw} = MNS(IPTP(X_H^{lin})) \quad (8)$$

where X_H^{lin} provides the supervision signal for the reconstruction of X_L^{raw} . A comprehensive overview of data synthesis is provided in Appendix A.1 and some visual examples of the synthetic data are found in Appendix A.4.

4 EXPERIMENTS

4.1 EXPERIMENTAL SETTINGS

Training and Testing Datasets. RDDM is trained on LSDIR Li et al. (2023) and a 10K-image subset of FFHQ Karras et al. (2019). The RVAE is trained on a broader collection including DIV2K Timofte et al. (2017), Flickr2K Agustsson & Timofte (2017), LSDIR Li et al. (2023), DIV8K Gu et al. (2019), and FFHQ Karras et al. (2019). RAW-domain training pairs are synthesized following the pipeline in Sec. 3.3. For evaluation, we employ both real-world and synthetic benchmarks. Real-world RAW testing is conducted on DND Plotz & Roth (2017), RealCapture Li et al. (2024), and SIDD Abdelhamed et al. (2018), covering diverse consumer cameras and mobile devices. Additionally, synthetic RAW benchmarks are constructed by applying our degradation method to HR images from DIV2K-Val Timofte et al. (2017), RealSR Cai et al. (2019), and DRealSR Wei et al. (2020).

Compared Methods. We compare RDDM against the best-performing traditional one-stage method and two-stage ISP→IR models methods, as shown in Table 1. For one-stage methods, we re-train JDnDmSR (Xing & Egiazarian), SwinIR (Liang et al., 2021), and MambaIRv2 (Guo et al., 2025) on the same RAW domain training dataset as our baseline. For two-stage ISP→IR methods, we choose PIPNet (A Sharif et al., 2021) as the DN and DM module for ISP and diffusion-based IR methods as our Real-IR baselines, including StableSR (Wang et al., 2024), DiffBIR (Lin et al., 2024), PASD (Yang et al., 2024), SeeSR (Wu et al., 2024b), SUPIR (Yu et al., 2024), and OSEDiff (Wu et al., 2024a). Additionally, we conduct a comparative analysis with GAN-based Real-IR methods, including BSRGAN Zhang et al. (2021), Real-ESRGAN Wang et al. (2021), LDL Liang et al. (2022), and FeMaSR Chen et al. (2022). The comparisons of RDDM against GAN-based Real-IR may be found in Appendix A.2

Table 1: Quantitative comparison with different methods on both synthetic benchmarks. The best, second best and third results of each metric are highlighted by red, orange and yellow cells respectively. \downarrow presents the smaller the better, \uparrow presents the bigger the better. Please note that we denote the number of sampling steps for each diffusion-based method using the format "method-steps".

Dataset	Method	PSNR \uparrow	SSIM \uparrow	LPIPS \downarrow	DISTS \downarrow	FID \downarrow	NIQE \downarrow	MUSIQ \uparrow	CLIQQA \uparrow
DIV2K-Val	JDnDmSR	23.4565	0.6192	0.5347	0.2655	45.3706	7.0895	32.1252	0.1978
	SwinIR	22.7983	0.6294	0.5345	0.2780	44.9270	7.1012	32.9053	0.2520
	MambaRv2	23.6377	0.6009	0.5882	0.2749	42.8625	7.2673	31.6576	0.2010
	ISP+StableSR-s200	23.6034	0.6133	0.4095	0.2092	35.6300	4.7840	43.8325	0.4284
	ISP+DiffBIR-s50	22.4903	0.5284	0.4519	0.2176	42.0167	4.6040	52.9640	0.6503
	ISP+PASD-s20	23.3860	0.6150	0.3029	0.1385	23.5801	3.4392	64.3181	0.6197
	ISP+SeeSR-s50	23.2836	0.6059	0.2880	0.1363	25.4424	3.5605	65.6650	0.6976
	ISP+SUPIR-s50	22.4837	0.5935	0.3265	0.1462	27.4418	3.5376	62.7078	0.5570
	ISP+OSEDiff-s1	22.5277	0.6069	0.2836	0.1351	38.0461	3.6427	66.2024	0.6818
	Ours-s1	23.7416	0.6296	0.2540	0.1197	23.8028	3.3627	65.4202	0.6737
DRealSR	JDnDmSR	27.6972	0.7995	0.3610	0.2210	31.1697	7.9294	30.4728	0.2373
	SwinIR	27.0657	0.8161	0.3714	0.2305	30.5639	7.5234	30.2268	0.2972
	MambaRv2	28.5563	0.7655	0.4409	0.2359	27.8182	8.1602	29.1201	0.2595
	ISP+StableSR-s200	27.1173	0.7613	0.3387	0.1978	25.8442	4.5959	49.2604	0.5991
	ISP+DiffBIR-s50	28.2670	0.7606	0.4142	0.2702	25.9530	6.3725	38.1396	0.5284
	ISP+PASD-s20	28.3377	0.7845	0.2870	0.1670	16.1714	4.6875	53.1539	0.5872
	ISP+SeeSR-s50	27.6513	0.7765	0.2972	0.1816	19.2938	4.2053	56.0800	0.6681
	ISP+SUPIR-s50	26.9559	0.7359	0.3262	0.1799	26.1866	5.0892	48.5114	0.4839
	ISP+OSEDiff-s1	25.1101	0.7315	0.3396	0.1900	32.4002	4.7336	57.3375	0.7376
	Ours-s1	28.3495	0.7892	0.2719	0.1649	17.4825	4.6852	57.0696	0.7035
RealSR	JDnDmSR	25.6346	0.7532	0.3649	0.2119	66.5709	7.4103	38.6661	0.2062
	SwinIR	25.4564	0.7477	0.3818	0.2283	67.1467	6.9218	38.5181	0.2637
	MambaRv2	25.6781	0.6976	0.4686	0.2399	64.8715	7.4959	36.2515	0.2100
	ISP+StableSR-s200	23.3339	0.6600	0.3505	0.1949	60.9322	3.9343	64.1478	0.6393
	ISP+DiffBIR-s50	25.3643	0.6761	0.4086	0.2478	56.7401	5.6140	49.4878	0.5581
	ISP+PASD-s20	24.8545	0.6886	0.3055	0.1720	40.8756	4.1290	63.5759	0.6223
	ISP+SeeSR-s50	24.8332	0.6957	0.2872	0.1807	36.0702	4.2017	66.3191	0.6977
	ISP+SUPIR-s50	23.9782	0.6505	0.3412	0.1937	51.7890	4.9086	59.3107	0.4814
	ISP+OSEDiff-s1	23.8067	0.6872	0.2988	0.1768	52.0761	4.2011	65.5805	0.6793
	Ours-s1	25.1264	0.7092	0.2546	0.1589	36.8671	4.1286	65.8881	0.6723

Evaluation Metrics. For a thorough assessment of the different methods, we utilize a variety of full-reference and non-reference evaluation metrics to test each method’s image fidelity and generation quality. PSNR and SSIM (Wang et al., 2004) (calculated on 3 channels) measure image fidelity, whereas LPIPS (Zhang et al., 2018a) and DISTS (Ding et al., 2020) measure perceptual qualities based on reference images. FID (Heusel et al., 2017) assesses the distributional distance between the GT and the restored images. NIQE (Mittal et al., 2012), MUSIQ (Ke et al., 2021), and CLIQQA (Wang et al., 2023) are non-reference image generation quality measurements.

Implementation Details. We train RDDM with the AdamW optimizer at a learning rate of $5e - 5$. The entire training process spans 150000 steps with a batch size of 16. The rank of LoRA in the RVAE Encoder and the diffusion network is set to 4. We employ DAPE as the sRGB domain text prompts extractor. We set $\lambda_1 = 1$, $\lambda_2 = 1$ and $\lambda_3 = 3$ for all experiments.

4.2 COMPARISONS WITH STATE-OF-THE-ARTS

Quantitative Comparisons on synthetic RAW benchmark. Table 1 presents the quantitative comparisons on three synthetic test datasets. RDDM ranks in the top 3 for all metrics, including PSNR, SSIM, LPIPS, DISTS, NIQE, MUSIQ, CLIQQA, and FID, across DIV2K-Val, DRealSR, and RealSR, except for PSNR on RealSR. JDnDmSR and SwinIR achieve slightly higher PSNR and SSIM on RealSR but significantly underperform on other metrics, particularly NIQE, MUSIQ, CLIQQA, and FID, indicating weaker generative capabilities. RDDM matches diffusion-based methods in generative performance while outperforming them in image fidelity metrics like PSNR and SSIM. Moreover, RDDM maintains the highest efficiency among diffusion-based competitors in terms of Params and FLOPs as shown in Table 2.

Qualitative Comparison on synthetic RAW benchmark. Visual comparisons on DIV2K-Val and DRealSR demonstrate RDDM’s superiority over existing one-stage and two-stage RAW-domain

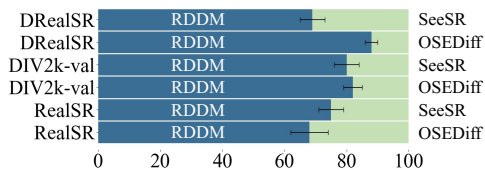


Figure 7: The user preference win rates of RDDM, compared to OSEDiff and SeeSR based on RealSR, DRealSR, and DIV2K-Val. We provide the 95% confidence interval of the win rate based on five independent annotation rounds.

Table 2: Comparisons of Params and FLOPs between RDDM and its competing methods on input resolution of 512×512 .

Method	Params(M)	FLOPs(G)
JDnDmSR	78.2	54
SwinIR	11.6	760
MambaIRv2	31.4	8260
ISP+StableSR-s200	1413	830
ISP+DiffBIR-s50	1673	1670
ISP+PASD-s20	1432	1590
ISP+SeeSR-s50	1622	1230
ISP+SUPIR-s50	4805	4100
ISP+OSEDiff-s1	1298	250
Ours-s1	1294	250

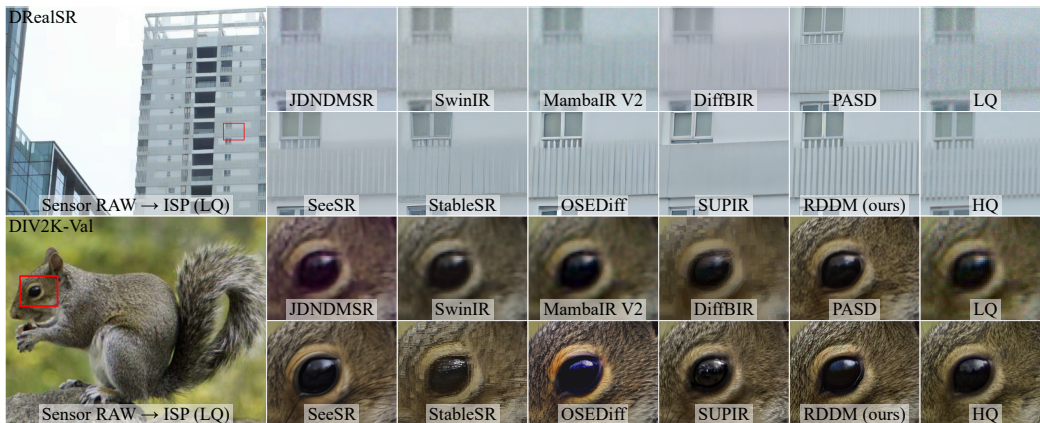


Figure 8: Qualitative comparison between RDDM and RAW domain one-stage method and two-stage ISP→IR methods on DRealSR dataset and DIV2K-Val dataset.

methods, as shown in Fig.8. While competitors like JDnDmSR and SwinIR suffer from blurriness and color bias, and diffusion-based models (e.g., SeeSR, OSEDiff) often fail to recover fine structures, RDDM reconstructs realistic, high-clarity textures. This confirms that RDDM effectively leverages RAW sensor signals to mitigate typical diffusion artifacts. More visualization comparison results are in the Appendix A.3. To further investigate the user preferences about these results, we conduct a user study on RealSR, DRealSR, and DIV2K-val test datasets, with 5 participants involved. For each set of comparison images, users select their preferred result. As shown in Fig. 7, the results demonstrate that our method significantly outperforms state-of-the-art methods in terms of perceptual quality.

Qualitative Comparison on real RAW benchmark. Visual comparisons on the DND dataset (Fig.9) highlight RDDM’s ability to recover clear and realistic structures on complex surfaces, whereas competing methods often over-smooth textures or fail to suppress noise. As depicted in Fig.10, on the multi-exposure SIDD dataset, RDDM consistently restores clean checkerboard patterns across varying exposure levels, avoiding the color deviations prevalent in one-stage models like MambaIR V2. Furthermore, RDDM exhibits robust generalization to unseen sensor patterns. When evaluated on the RealCapture dataset (RGBG Bayer pattern), RDDM successfully uncovers fine foliage and wall details, as illustrated in Fig.11. In contrast, alternative methods suffer from severe residual noise, grid artifacts, and detail loss, confirming RDDM’s superior cross-sensor adaptability.

4.3 ABLATION STUDY

The Importance of RVAE. To identify the optimal RVAE architecture and training protocol, we conduct a comprehensive evaluation of six adaptation strategies for RAW-domain reconstruction. The qualitative and quantitative results are summarized as follows:



Figure 9: Qualitative comparison between RDDM and RAW domain one-stage method and two-stage ISP→IR methods on the real RAW DND dataset.

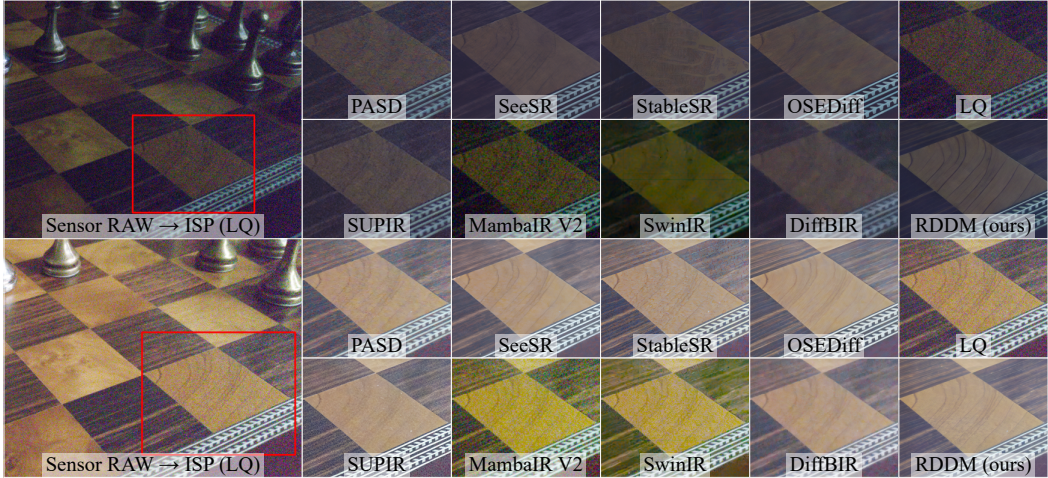


Figure 10: Qualitative comparison between RDDM and RAW domain one-stage method and two-stage ISP→IR methods on the real RAW SIDD dataset.

(i) *Baseline Adaptations (Settings 1–2)*: directly employing a pre-trained sRGB VAE or training from scratch yields either severe degradation or persistent mosaic artifacts (Fig.12a-b).

(ii) *LoRA-based Fine-tuning (Settings 3–5)*: furthermore, fine-tuning only the encoder, decoder, or both via LoRA proves insufficient to bridge the domain gap between sRGB and RAW, as mosaic patterns remain prominent (Fig.12c-e).

(iii) *Proposed Joint Training (Setting 6)*: the optimal strategy involves freezing a pre-trained linear domain decoder while jointly optimizing the encoder and diffusion network via LoRA. This configuration effectively eliminates artifacts, as demonstrated in Fig.12(f).

Quantitative metrics in Table 3 further validate that Setting 6 achieves the highest reconstruction fidelity. Furthermore, End-to-end evaluations within the RDDM framework (Table 4) confirm that our RVAE strategy provides the most robust foundation for high-quality RAW-to-linear restoration, significantly outperforming alternative adaptation protocols. Moreover, Fig.13 confirms that RVAE effectively mitigates chromatic deviations.

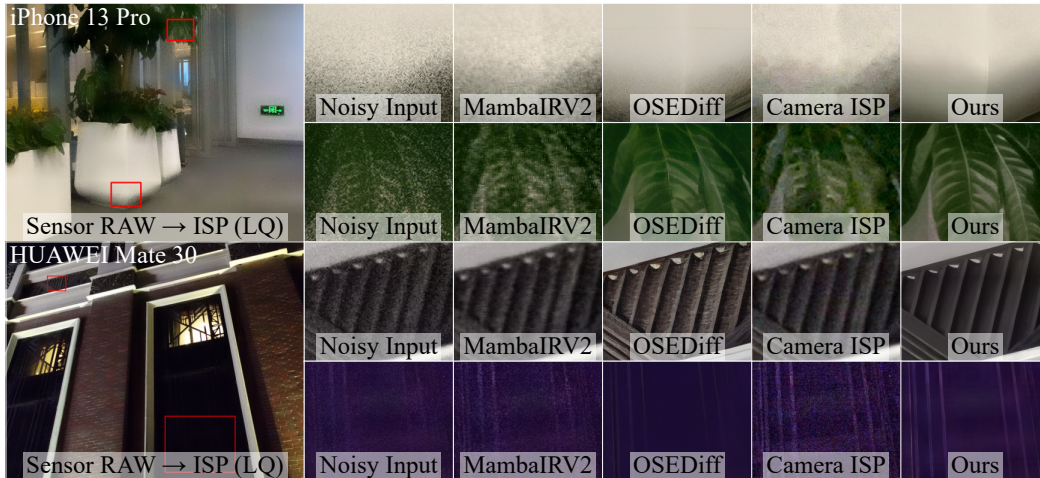


Figure 11: Qualitative comparison between RDDM and RAW domain one-stage method and two-stage ISP→IR methods on the real RAW RealCapture dataset. The results in the last row are brightened to provide a clearer visualization of the restored details.

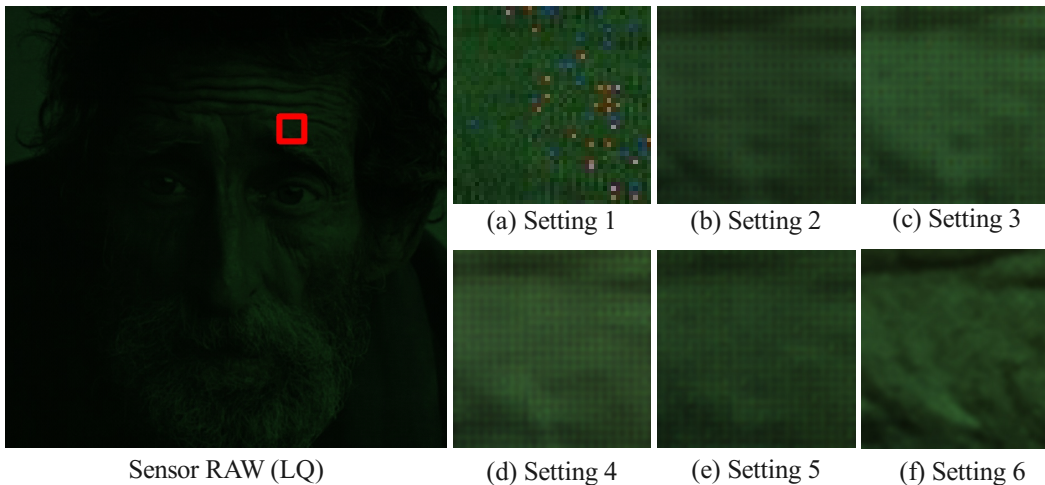


Figure 12: Qualitative comparison of different VAE settings on the RealSR benchmark. Setting 6 (ours) achieves the optimal performance.



Figure 13: Qualitative comparison of sRGB VAE and RVAE on the RealSR benchmark.

Table 3: Quantitative reconstruction performance of different VAE settings on RealSR.

Setting	PSNR↑	SSIM↑	LPIPS↓	FID↓
1	25.2625	0.8017	0.1719	41.8118
2	27.1487	0.7035	0.3068	48.4675
3	27.6892	0.7176	0.2787	38.2007
4	26.3147	0.6703	0.3967	53.4004
5	25.4509	0.6277	0.4533	64.2444
6	32.5424	0.9082	0.0533	11.6156

The Necessity of CMB-LoRA. We investigate the parameter-sharing strategy within the CMB-LoRA module by comparing our pattern-specific design against a shared-weight baseline. As reported in Table 5, the shared configuration leads to performance degradation across diverse sensor layouts. This decline stems from the inherent spatial disparities among heterogeneous Bayer patterns (e.g., RGGB, BGGR, and RGBG). While a single weight matrix struggles to capture such diverse local structural characteristics, our pattern-specific design provides the necessary flexibility

Table 4: Quantitative performance of RDDM with different VAE settings on the RealSR dataset.

Setting	PSNR \uparrow	SSIM \uparrow	LPIPS \downarrow	DISTS \downarrow	FID \downarrow	NIQE \downarrow	MUSIQ \uparrow	CLIPQA \uparrow
1	20.5609	0.5797	0.3930	0.2071	73.5659	4.0762	62.7875	0.6431
2	22.3752	0.6484	0.4785	0.3307	138.4347	6.5993	47.2304	0.4233
3	21.0398	0.6115	0.5710	0.4235	143.3710	10.5422	37.3569	0.3745
4	21.3850	0.6080	0.4250	0.2901	108.3618	7.5271	52.8636	0.2931
5	21.3886	0.5732	0.4911	0.3166	135.6228	7.5537	38.7119	0.1483
6	25.1264	0.7092	0.2546	0.1589	36.8671	4.1286	65.8881	0.6723

Table 5: Comparison of CMB LoRA and All-in-One LoRA on RealSR benchmark.

	PSNR \uparrow	SSIM \uparrow	LPIPS \downarrow	DISTS \downarrow	FID \downarrow	NIQE \downarrow	MUSIQ \uparrow	CLIPQA \uparrow
All-in-One LoRA	24.5355	0.7003	0.2550	0.1555	40.6767	4.1165	65.0143	0.6660
CMB-LoRA	25.1264	0.7092	0.2546	0.1589	36.8671	4.1286	65.8881	0.6723



Figure 14: Qualitative comparison of RAW, sRGB, and dual domain loss on the DIV2K-Val.

to model the unique statistical distributions of each RAW format, ensuring robust adaptation across heterogeneous sensors.

The Effectiveness of Dual Domain Loss. We evaluate the impact of domain-specific losses in Table 6. Exclusively RAW-domain training (Setting 1) yields high non-reference scores (e.g., MUSIQ, CLIPQA) but introduces chromatic artifacts due to the lack of color constraints. Conversely, sRGB-only optimization (Setting 2) ensures color consistency but sacrifices structural fidelity by discarding sensor-level signals. By imposing dual-domain supervision, RDDM achieves an optimal trade-off between structural authenticity and visual realism. As illustrated in Fig.14, while this strategy shows a marginal decline in reference-less metrics, which often over-reward texture intensity, it significantly improves global color stability and alignment with the ground truth, prioritizing holistic fidelity over local high-frequency noise.

The Comparison of Text Prompt Extractors. To evaluate the efficacy of our proposed RPE, we compare it against two alternative prompt-extraction strategies: (1) Direct sRGB-Extractor, which utilizes a pre-trained sRGB model on RAW data; and (2) ISP-based Conversion, which extracts prompts from RAW images pre-processed by a standard ISP. As summarized in Table 7, the proposed RPE consistently outperforms both baselines across all metrics, including reconstruction fidelity (PSNR, DISTS) and perceptual quality (FID, NIQE, MUSIQ, CLIPQA). By generating more precise prompts, RPE effectively activates the rich generative priors of the diffusion model, facilitating high-fidelity restoration and superior detail synthesis that standard or ISP-processed extractors fail to achieve.

5 CONCLUSION

In this paper, we present RDDM, a pioneering paradigm for Real-IR that operates directly from sensor RAW data. By integrating the robust generative priors of the diffusion model, RVAE with a specialized CMB-LoRA module, RDDM effectively addresses the inherent limitations of traditional sRGB-based restoration. Unlike conventional methods that struggle with the information loss incurred by irreversible ISP pipelines, our approach leverages the unprocessed native signal of RAW

Table 6: Comparison of different domain losses on the DIV2K benchmark.

RAW Loss	sRGB Loss	PSNR \uparrow	SSIM \uparrow	LPIPS \downarrow	DISTS \downarrow	FID \downarrow	NIQE \downarrow	MUSIQ \uparrow	CLIPQA \uparrow
✓	×	22.9510	0.6096	0.2794	0.1337	36.3172	3.4637	66.1391	0.7298
×	✓	23.3129	0.6237	0.2635	0.1216	29.5131	3.3352	64.7748	0.6637
✓	✓	23.7416	0.6296	0.2540	0.1197	23.8028	3.3627	65.4202	0.6737

Table 7: Comparison of different text prompt extractors on the RealSR benchmark.

	PSNR \uparrow	SSIM \uparrow	LPIPS \downarrow	DISTS \downarrow	FID \downarrow	NIQE \downarrow	MUSIQ \uparrow	CLIPQA \uparrow
sRGBPE	24.7811	0.7201	0.2495	0.1601	38.1092	4.2538	65.4506	0.6579
ISPPE	24.7816	0.7201	0.2495	0.1600	38.0969	4.2539	65.4526	0.6579
RPE	25.1264	0.7092	0.2546	0.1589	36.8671	4.1286	65.8881	0.6723

images to recover superior structural details and textures. While the current $8\times$ down-sampling architecture inherited from Stable Diffusion 2.1 imposes certain constraints on fine-scale fidelity. Future research will focus on developing VAE encode strategies to further preserve sub-pixel spatial information and push the boundaries of high-fidelity Real-IR.

REFERENCES

- SM A Sharif, Rizwan Ali Naqvi, and Mithun Biswas. Beyond joint demosaicking and denoising: An image processing pipeline for a pixel-bin image sensor. In *Proceedings of the IEEE/CVF conference on computer vision and pattern recognition*, pp. 233–242, 2021.
- Abdelrahman Abdelhamed, Stephen Lin, and Michael S. Brown. A high-quality denoising dataset for smartphone cameras. In *IEEE Conference on Computer Vision and Pattern Recognition (CVPR)*, June 2018.
- Eirikur Agustsson and Radu Timofte. Ntire 2017 challenge on single image super-resolution: Dataset and study. In *Proceedings of the IEEE conference on computer vision and pattern recognition workshops*, pp. 126–135, 2017.
- Tim Brooks, Ben Mildenhall, Tianfan Xue, Jiawen Chen, Dillon Sharlet, and Jonathan T Barron. Unprocessing images for learned raw denoising. In *Proceedings of the IEEE/CVF conference on computer vision and pattern recognition*, pp. 11036–11045, 2019.
- Jianrui Cai, Hui Zeng, Hongwei Yong, Zisheng Cao, and Lei Zhang. Toward real-world single image super-resolution: A new benchmark and a new model. In *Proceedings of the IEEE/CVF international conference on computer vision*, pp. 3086–3095, 2019.
- Chaofeng Chen, Xinyu Shi, Yipeng Qin, Xiaoming Li, Xiaoguang Han, Tao Yang, and Shihui Guo. Real-world blind super-resolution via feature matching with implicit high-resolution priors. In *Proceedings of the 30th ACM International Conference on Multimedia*, pp. 1329–1338, 2022.
- Keyan Ding, Kede Ma, Shiqi Wang, and Eero P Simoncelli. Image quality assessment: Unifying structure and texture similarity. *IEEE transactions on pattern analysis and machine intelligence*, 44(5):2567–2581, 2020.
- Yuchen Fan, Jiahui Yu, Yiqun Mei, Yulun Zhang, Yun Fu, Ding Liu, and Thomas S Huang. Neural sparse representation for image restoration. *Advances in Neural Information Processing Systems*, 33:15394–15404, 2020.
- Shuhang Gu, Andreas Lugmayr, Martin Danelljan, Manuel Fritsche, Julien Lamour, and Radu Timofte. Div8k: Diverse 8k resolution image dataset. In *2019 IEEE/CVF International Conference on Computer Vision Workshop (ICCVW)*, pp. 3512–3516. IEEE, 2019.
- Hang Guo, Yong Guo, Yaohua Zha, Yulun Zhang, Wenbo Li, Tao Dai, Shu-Tao Xia, and Yawei Li. Mambairv2: Attentive state space restoration. In *Proceedings of the Computer Vision and Pattern Recognition Conference*, pp. 28124–28133, 2025.
- Martin Heusel, Hubert Ramsauer, Thomas Unterthiner, Bernhard Nessler, and Sepp Hochreiter. Gans trained by a two time-scale update rule converge to a local nash equilibrium. *Advances in neural information processing systems*, 30, 2017.
- Edward J Hu, Yelong Shen, Phillip Wallis, Zeyuan Allen-Zhu, Yuanzhi Li, Shean Wang, Lu Wang, Weizhu Chen, et al. Lora: Low-rank adaptation of large language models. *ICLR*, 1(2):3, 2022.
- Gu Jinjin, Cai Haoming, Chen Haoyu, Ye Xiaoxing, Jimmy S Ren, and Dong Chao. Pipal: a large-scale image quality assessment dataset for perceptual image restoration. In *Computer Vision—ECCV 2020: 16th European Conference, Glasgow, UK, August 23–28, 2020, Proceedings, Part XI 16*, pp. 633–651. Springer, 2020.
- Tero Karras, Samuli Laine, and Timo Aila. A style-based generator architecture for generative adversarial networks. In *Proceedings of the IEEE/CVF conference on computer vision and pattern recognition*, pp. 4401–4410, 2019.
- Junjie Ke, Qifei Wang, Yilin Wang, Peyman Milanfar, and Feng Yang. Musiq: Multi-scale image quality transformer. In *Proceedings of the IEEE/CVF international conference on computer vision*, pp. 5148–5157, 2021.

-
- Christian Ledig, Lucas Theis, Ferenc Huszár, Jose Caballero, Andrew Cunningham, Alejandro Acosta, Andrew Aitken, Alykhan Tejani, Johannes Totz, Zehan Wang, et al. Photo-realistic single image super-resolution using a generative adversarial network. In *Proceedings of the IEEE conference on computer vision and pattern recognition*, pp. 4681–4690, 2017.
- Ruikang Li, Yujin Wang, Shiqi Chen, Fan Zhang, Jinwei Gu, and Tianfan Xue. Dualdn: Dual-domain denoising via differentiable isp. In *European Conference on Computer Vision*, pp. 160–177. Springer, 2024.
- Yawei Li, Kai Zhang, Jingyun Liang, Jiezhong Cao, Ce Liu, Rui Gong, Yulun Zhang, Hao Tang, Yun Liu, Denis Demandolx, et al. Lsdnr: A large scale dataset for image restoration. In *Proceedings of the IEEE/CVF Conference on Computer Vision and Pattern Recognition*, pp. 1775–1787, 2023.
- Jie Liang, Hui Zeng, and Lei Zhang. Details or artifacts: A locally discriminative learning approach to realistic image super-resolution. In *Proceedings of the IEEE/CVF conference on computer vision and pattern recognition*, pp. 5657–5666, 2022.
- Jingyun Liang, Jiezhong Cao, Guolei Sun, Kai Zhang, Luc Van Gool, and Radu Timofte. Swinir: Image restoration using swin transformer. In *Proceedings of the IEEE/CVF international conference on computer vision*, pp. 1833–1844, 2021.
- Xinqi Lin, Jingwen He, Ziyang Chen, Zhaoyang Lyu, Bo Dai, Fanghua Yu, Yu Qiao, Wanli Ouyang, and Chao Dong. Diffbir: Toward blind image restoration with generative diffusion prior. In *European Conference on Computer Vision*, pp. 430–448. Springer, 2024.
- Anish Mittal, Rajiv Soundararajan, and Alan C Bovik. Making a “completely blind” image quality analyzer. *IEEE Signal processing letters*, 20(3):209–212, 2012.
- Rang MH Nguyen and Michael S Brown. Raw image reconstruction using a self-contained srgb-jpeg image with only 64 kb overhead. In *Proceedings of the IEEE conference on computer vision and pattern recognition*, pp. 1655–1663, 2016.
- Tobias Plotz and Stefan Roth. Benchmarking denoising algorithms with real photographs. In *Proceedings of the IEEE conference on computer vision and pattern recognition*, pp. 1586–1595, 2017.
- Dustin Podell, Zion English, Kyle Lacey, Andreas Blattmann, Tim Dockhorn, Jonas Müller, Joe Penna, and Robin Rombach. Sdxl: Improving latent diffusion models for high-resolution image synthesis. *arXiv preprint arXiv:2307.01952*, 2023.
- Robin Rombach, Andreas Blattmann, Dominik Lorenz, Patrick Esser, and Björn Ommer. High-resolution image synthesis with latent diffusion models. In *Proceedings of the IEEE/CVF conference on computer vision and pattern recognition*, pp. 10684–10695, 2022.
- Radu Timofte, Eirikur Agustsson, Luc Van Gool, Ming-Hsuan Yang, and Lei Zhang. Ntire 2017 challenge on single image super-resolution: Methods and results. In *Proceedings of the IEEE conference on computer vision and pattern recognition workshops*, pp. 114–125, 2017.
- Jiayin Wang, Kelvin CK Chan, and Chen Change Loy. Exploring clip for assessing the look and feel of images. In *Proceedings of the AAAI conference on artificial intelligence*, volume 37, pp. 2555–2563, 2023.
- Jiayin Wang, Zongsheng Yue, Shangchen Zhou, Kelvin CK Chan, and Chen Change Loy. Exploiting diffusion prior for real-world image super-resolution. *International Journal of Computer Vision*, 132(12):5929–5949, 2024.
- Xintao Wang, Ke Yu, Shixiang Wu, Jinjin Gu, Yihao Liu, Chao Dong, Yu Qiao, and Chen Change Loy. ESRGAN: Enhanced super-resolution generative adversarial networks. In *Proceedings of the European conference on computer vision (ECCV) workshops*, pp. 0–0, 2018.
- Xintao Wang, Liangbin Xie, Chao Dong, and Ying Shan. Real-esrgan: Training real-world blind super-resolution with pure synthetic data. In *Proceedings of the IEEE/CVF international conference on computer vision*, pp. 1905–1914, 2021.

-
- Zhou Wang, Alan C Bovik, Hamid R Sheikh, and Eero P Simoncelli. Image quality assessment: from error visibility to structural similarity. *IEEE transactions on image processing*, 13(4):600–612, 2004.
- Pengxu Wei, Ziwei Xie, Hannan Lu, Zongyuan Zhan, Qixiang Ye, Wangmeng Zuo, and Liang Lin. Component divide-and-conquer for real-world image super-resolution. In *European conference on computer vision*, pp. 101–117. Springer, 2020.
- Rongyuan Wu, Lingchen Sun, Zhiyuan Ma, and Lei Zhang. One-step effective diffusion network for real-world image super-resolution. *Advances in Neural Information Processing Systems*, 37: 92529–92553, 2024a.
- Rongyuan Wu, Tao Yang, Lingchen Sun, Zhengqiang Zhang, Shuai Li, and Lei Zhang. Seesr: Towards semantics-aware real-world image super-resolution. In *Proceedings of the IEEE/CVF conference on computer vision and pattern recognition*, pp. 25456–25467, 2024b.
- Liangbin Xie, Xintao Wang, Xiangyu Chen, Gen Li, Ying Shan, Jiantao Zhou, and Chao Dong. Desra: detect and delete the artifacts of gan-based real-world super-resolution models. *arXiv preprint arXiv:2307.02457*, 2023.
- Wenzhu Xing and Karen Egiazarian. End-to-end learning for joint image demosaicing, denoising and super-resolution supplementary material.
- Yazhou Xing, Zian Qian, and Qifeng Chen. Invertible image signal processing. In *Proceedings of the IEEE/CVF conference on computer vision and pattern recognition*, pp. 6287–6296, 2021.
- Tao Yang, Rongyuan Wu, Peiran Ren, Xuansong Xie, and Lei Zhang. Pixel-aware stable diffusion for realistic image super-resolution and personalized stylization. In *European conference on computer vision*, pp. 74–91. Springer, 2024.
- Fanghua Yu, Jinjin Gu, Zheyuan Li, Jinfan Hu, Xiangtao Kong, Xintao Wang, Jingwen He, Yu Qiao, and Chao Dong. Scaling up to excellence: Practicing model scaling for photo-realistic image restoration in the wild. In *Proceedings of the IEEE/CVF Conference on Computer Vision and Pattern Recognition*, pp. 25669–25680, 2024.
- Jiale Zhang, Yulun Zhang, Jinjin Gu, Yongbing Zhang, Linghe Kong, and Xin Yuan. Accurate image restoration with attention retractable transformer. *arXiv preprint arXiv:2210.01427*, 2022.
- Kai Zhang, Wangmeng Zuo, Shuhang Gu, and Lei Zhang. Learning deep cnn denoiser prior for image restoration. In *Proceedings of the IEEE conference on computer vision and pattern recognition*, pp. 3929–3938, 2017.
- Kai Zhang, Jingyun Liang, Luc Van Gool, and Radu Timofte. Designing a practical degradation model for deep blind image super-resolution. In *Proceedings of the IEEE/CVF international conference on computer vision*, pp. 4791–4800, 2021.
- Lvmin Zhang, Anyi Rao, and Maneesh Agrawala. Adding conditional control to text-to-image diffusion models. In *Proceedings of the IEEE/CVF international conference on computer vision*, pp. 3836–3847, 2023.
- Richard Zhang, Phillip Isola, Alexei A Efros, Eli Shechtman, and Oliver Wang. The unreasonable effectiveness of deep features as a perceptual metric. In *Proceedings of the IEEE conference on computer vision and pattern recognition*, pp. 586–595, 2018a.
- Yulun Zhang, Yapeng Tian, Yu Kong, Bineng Zhong, and Yun Fu. Residual dense network for image super-resolution. In *Proceedings of the IEEE conference on computer vision and pattern recognition*, pp. 2472–2481, 2018b.
- Yulun Zhang, Kunpeng Li, Kai Li, Bineng Zhong, and Yun Fu. Residual non-local attention networks for image restoration. *arXiv preprint arXiv:1903.10082*, 2019.
- Chuanyang Zheng, Yihang Gao, Han Shi, Minbin Huang, Jingyao Li, Jing Xiong, Xiaozhe Ren, Michael Ng, Xin Jiang, Zhenguo Li, et al. Dape: Data-adaptive positional encoding for length extrapolation. *Advances in Neural Information Processing Systems*, 37:26659–26700, 2024.

A APPENDIX

The appendix provides additional technical details, experimental results, and visual comparisons to support the main paper. Specifically, it includes:

- Additional demonstrations regarding ISP and inverse ISP (referring to Sections 3.1 and 3.3 in the main paper).
- Comparisons against GAN-based methods (referring to Section 4.2 in the main paper).
- More qualitative comparisons (referring to Section 4.2 in the main paper).
- Visualizations of some examples of the synthetic RAW data. (referring to Section 3.3 in the main paper).

A.1 ISP AND INVERSE ISP

ISP and Inverse ISP. The RAW sensor data obtained by a camera is fundamentally different from the sRGB images, which closely resemble human visual perception. Indeed, it is necessary to process RAW images through an ISP to obtain the final sRGB images. Fig.15 illustrates the processing pipelines of ISP and InverseISP. We modify the InverseISP of Brooks et al. (2019) and propose a differentiable ISP approach that can map the model’s output to the sRGB domain for optimization. During the ISP process, denoising and demosaicing are ill-posed problems, and we optimize these two tasks jointly with the Real-IR task. Above all, in the ISP process, the Automatic White Balance (AWB) algorithm multiplies the red and blue channels by gains to produce an image that appears to be lit under “neutral” illumination, which can be formulated as Equation 9:

$$\begin{aligned} x_L^{awb} &= X_L^{nm} \odot M_{gain} \\ x_L^{nm} &= X_L^{awb} \odot \frac{1}{M_{gain}} \end{aligned} \quad (9)$$

where x_L^{awb} , X_L^{nm} , and M_{gain} are the linear-domain image processed by AWB, the linear image processed by denoising and demosaicing, and the pixel-wise channel gain, respectively.

Secondly, the color correction algorithm converts its own “camera space” sRGB color measurements to sRGB values by a color correction matrix as shown in Equation 10:

$$\begin{aligned} x_L^{ccm} &= x_L^{awb} \times M_c \\ x_L^{awb} &= x_L^{ccm} \times M_c^{-1} \end{aligned} \quad (10)$$

where x_L^{ccm} , M_c are the linear-domain image processed by the CCM algorithm and the color correction matrix, respectively.

Thirdly, since humans are more sensitive to gradations in the dark areas of images, gamma compression is typically used to allocate more bits of dynamic range to low-intensity pixels as stated in Equation 11:

$$\begin{aligned} X_L^{gamma} &= \max(x_L^{ccm}, \epsilon)^{1/2.2} \\ X_L^{ccm} &= \max(x_L^{gamma}, \epsilon)^{2.2} \end{aligned} \quad (11)$$

Note that we set $\epsilon = 10^{-8}$ to prevent numerical instability during training.

InverseISP is the inverse process of ISP, where the mosaicing algorithm acquires the RAW image $X_L^{raw} \in \mathcal{R}^{h \times w \times 1}$ with a CFA by extracting the corresponding pixel values from the three channels. The noise in RAW images mainly comes from two sources: photon arrival statistics (shot noise) and imprecision in the readout circuitry (read noise). We can approximate these two types of noise as a single heteroscedastic Gaussian distribution defined in Equation 12:

$$y \sim \mathcal{N}(\mu = 0, \sigma^2 = \lambda_{shot} X_L^{mosaic} + \lambda_{read}) \quad (12)$$

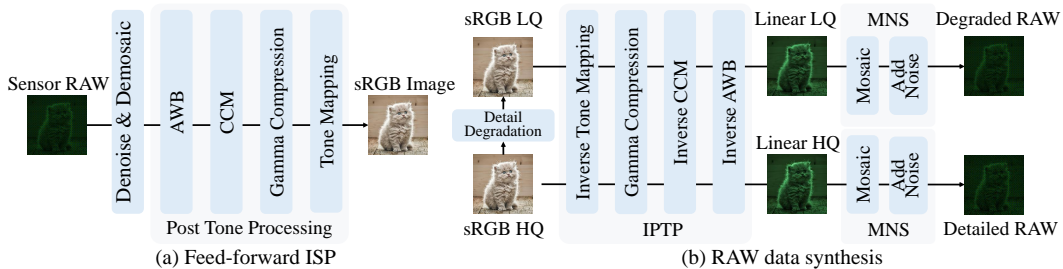


Figure 15: The ISP pipeline and the data synthesis pipeline.

Dataset	Method	PSNR \uparrow	SSIM \uparrow	LPIPS \downarrow	DISTS \downarrow	FID \downarrow	NIQE \downarrow	MUSIQ \uparrow	CLIPQA \uparrow
DIV2K-Val	ISP+BSRGAN	24.4124	0.6500	0.4174	0.2173	33.8937	5.1222	44.2923	0.4580
	ISP+Real-ESRGAN	24.2373	0.6426	0.3888	0.2007	35.3941	4.8658	48.6062	0.5157
	ISP+LDL	24.2922	0.6243	0.4684	0.2540	34.9855	5.5153	29.8086	0.3714
	ISP+FeMaSR	23.5889	0.6066	0.4347	0.2273	34.9390	5.7403	43.3786	0.5187
	Ours	23.7416	0.6296	0.2540	0.1197	23.8028	3.3627	65.4202	0.6737
DRealSR	ISP+BSRGAN	30.1134	0.8282	0.3196	0.1982	20.5962	5.6748	42.4667	0.5105
	ISP+Real-ESRGAN	29.1309	0.8055	0.3361	0.2042	23.5094	5.5440	46.0976	0.5548
	ISP+LDL	29.9312	0.7967	0.3640	0.2173	20.9155	5.9973	29.3485	0.4047
	ISP+FeMaSR	28.1176	0.7460	0.4007	0.2356	24.3254	6.3530	41.3755	0.5844
	Ours	28.3495	0.7892	0.2719	0.1649	17.4825	4.6852	57.0696	0.7035
RealSR	ISP+BSRGAN	27.0999	0.7648	0.3190	0.1984	50.7266	5.0958	50.2340	0.5052
	ISP+Real-ESRGAN	26.3844	0.7474	0.3332	0.1995	49.3939	4.5754	55.7670	0.5498
	ISP+LDL	26.5426	0.7186	0.3871	0.2141	53.1533	5.2573	33.9660	0.3656
	ISP+FeMaSR	25.5820	0.6898	0.3891	0.2278	53.7582	5.8086	51.1097	0.5917
	Ours	25.1264	0.7092	0.2546	0.1589	36.8671	4.1286	65.8881	0.6723

Table 8: Quantitative comparison with different methods on both synthetic benchmarks. \downarrow presents the smaller the better, \uparrow presents the bigger the better. Our method RDDM exceeds its competing models in terms of image fidelity, while maintaining a satisfactory image generation ability approximately equivalent to the other baselines.

The linear-domain image is obtained by Equation 13:

$$X_L^{RAW} = X_L^{mosaic} + y \quad (13)$$

where X_L^{mosaic} is the RAW image processed by mosaic algorithm and y is the noise intensity added onto X_L^{mosaic} to obtain the Sensor RAW X_L^{RAW} . λ_{shot} and λ_{read} are the function of ISO light sensitivity level.

A.2 QUANTITATIVE COMPARISONS WITH GAN-BASED METHODS

We compare RDDM against four two-stage ISP \rightarrow GAN-based-IR methods. For the first ISP stage, we again use PIPNet A Sharif et al. (2021) as the DN and DM module; for the second IR stage, we use BSRGAN Zhang et al. (2021), Real-ESRGAN Wang et al. (2021), LDL Liang et al. (2022), and FeMaSR Chen et al. (2022) as our baselines. The results are shown in Table 8. Admittedly, two-stage methods involving GAN-based IR models demonstrate better fidelity results as expected, i.e., higher PSNR and SSIM metrics. However, their image generation capability is far behind RDDM. Visualization comparisons are shown in Fig. 16.

A.3 MORE QUALITATIVE COMPARISONS

To further demonstrate the perceptual superiority of our approach, we provide extended qualitative comparisons in Fig. 17. These comparisons encompass both RAW-domain one-stage methods and representative two-stage pipelines (i.e., ISP followed by sRGB domain IR). The visual results across diverse challenging scenarios consistently showcase that RDDM achieves superior texture restoration and color fidelity, effectively mitigating the artifacts typically found in traditional multi-stage processing.

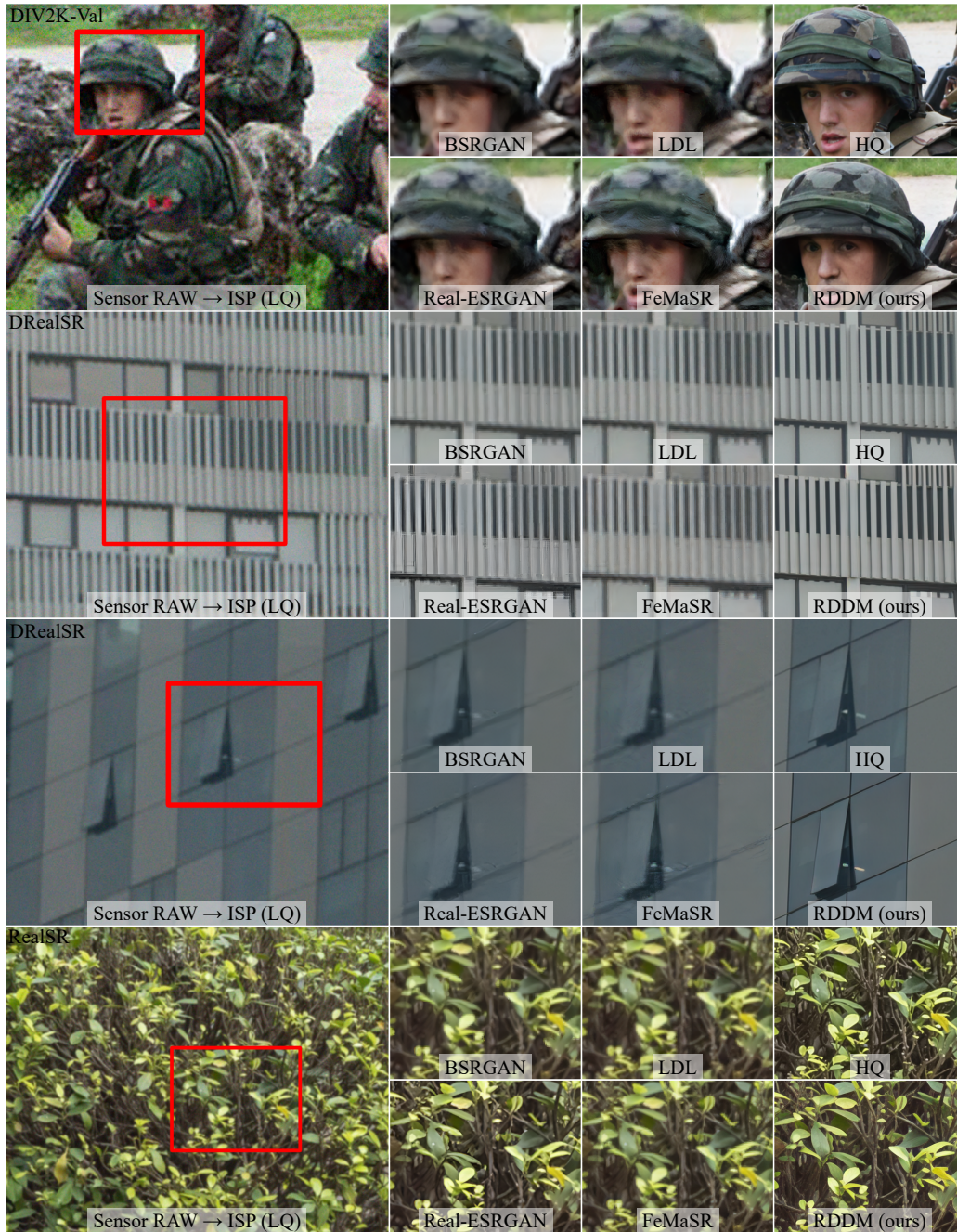


Figure 16: Qualitative comparison between RDDM and GAN-based methods on DIV2K-Val, DRealSR and RealSR dataset.

A.4 EXAMPLES OF SYNTHETIC RAW DATA

Following the data synthesis pipeline detailed in Fig.15, we provide representative examples of our synthesized RAW images in Fig.18. These samples visually demonstrate that our pipeline effectively simulates realistic sensor noise and Bayer mosaics. By bridging the gap between synthetic degradations and real-world RAW characteristics, these generated images provide high-quality supervision, which is fundamental to the robust performance of RDDM.

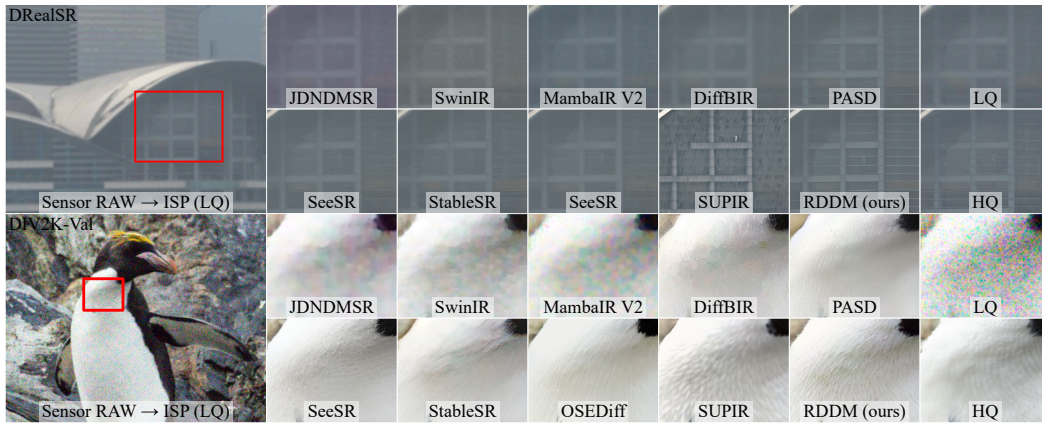


Figure 17: Qualitative comparison between RDDM and RAW domain one-stage method and two-stage ISP→IR methods on DRealSR dataset and DIV2K-Val dataset.

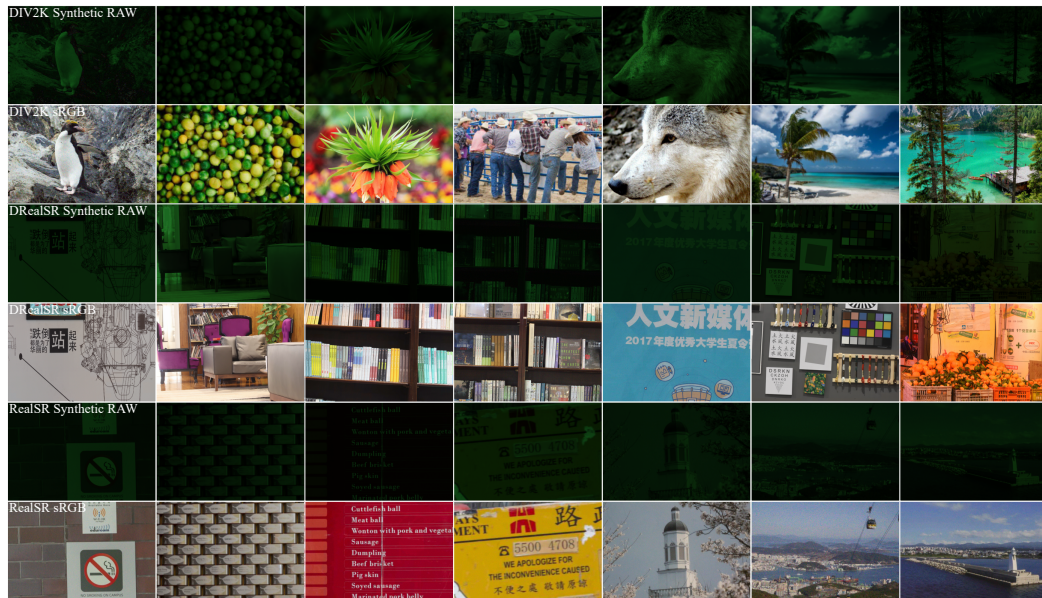


Figure 18: Examples of synthetic RAW data produced by our data synthesis pipeline. From top to bottom, each row represents the RAW data from DIV2K, the corresponding sRGB data from DIV2K, the RAW data from DRealSR, the corresponding sRGB data from DRealSR, the RAW data from RealSR and the corresponding sRGB data from RealSR.